Performance enhancement of a C-shaped printed circuit heat exchanger in supercritical CO2 Brayton cycle: A machine learning-based optimization study

DOI:
10.1016/j.csite.2022.102276

Case Studies in Thermal Engineering 38 (2022) 102276

Contents lists available at ScienceDirect

Case Studies in Thermal Engineering

journal homepage: www.elsevier.com/locate/csite

Performance enhancement of a C-shaped printed circuit heat exchanger in supercritical CO_2 Brayton cycle: A machine learning-based optimization study

Muhammad Saeed [a,c,*], Abdallah S. Berrouk [a,b], Yasser F. Al Wahedi [c], Munendra Pal Singh [a], Ibragim Abu Dagga [a], Imran Afgan [a]

[a] Mechanical Engineering Department, Khalifa University of Science and Technology, P.O. Box 127788, Abu Dhabi, United Arab Emirates
[b] Center for Catalysis and Separation (CeCas), Khalifa University of Science and Technology, P.O. Box 127788, Abu Dhabi, United Arab Emirates
[c] Abu Dhabi Maritime Academy, Abu Dhabi, P.O. Box 54477, United Arab Emirates

GRAPHICAL ABSTRACT

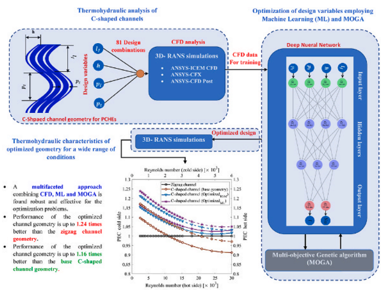

ARTICLE INFO

Keywords:
sCO_2 Brayton cycle
Printed circuit heat exchangers
Machine learning
Deep neural network
Thermal-hydraulic performance

ABSTRACT

The present work is focused on enhancing the overall thermo-hydraulic performance of a previously proposed C-shaped printed circuit heat exchanger (PCHEs) using Machine Learning (ML) Algorithms. In this context, CFD analysis is carried out on 81 different channel configurations of the C-shaped channel geometry, and computed data is used to train three ML algorithms. Later, C-shaped channel geometry is optimized by coupling the trained ML model with the multi-objective genetic algorithm (MOGA). Finally, the optimized channel geometry (called optimized$_{ML}$) is investigated numerically for a wide range of Reynolds numbers. Its performance is compared with the zigzag geometry, C-shaped base geometry, and previously optimized C-shape channel geometry using response surface methodology (RSM). The findings showed that the multilayered approach combining MOGA, CFD, and machine learning techniques is beneficial to accomplish a

* Corresponding author. Mechanical Engineering Department, Khalifa University of Science and Technology, P.O. Box 127788, Abu Dhabi, United Arab Emirates.
E-mail address: muhammad.saeed@safeen.ae (M. Saeed).

https://doi.org/10.1016/j.csite.2022.102276
Received 6 February 2022; Received in revised form 17 June 2022; Accepted 6 July 2022
Available online 8 August 2022
2214-157X/

robust and realistic optimized solution. Comparing the thermo-hydraulic characteristics of the optimized$_{ML}$ channel geometry with zigzag channel geometry shows that the former is up to 1.24 times better than the latter based on the performance evaluation criteria (PEC). Furthermore, the overall performance of the optimize^{ML} channel geometry was found up to 21% and 16% higher than the optimized $_{RSM}$ geometry on the cold and hot sides, respectively.

Nomenclature

C_p	specific heat capacity [J. kg^{-1}.K^{-1}]
D_h	hydraulic diameter [mm]
f	friction factor
h	channel depth [mm], enthalpy [J. kg^{-1}], local heat transfer coefficient [$W\,m^{-2}K^{-1}$]
k	thermal conductivity [W m^{-1}K^{-1}]
l_f	length of fin [mm]
$\dot{m}$	mass flow rate [kg s^{-1}]
Nu	Nusselt number
p	pressure [Pa]
p_l	longitudinal pitch [mm]
p_t	transverse pitch [mm]
Re	Reynolds number
n	normal vector
q	Heat flux [$J.\,m^{-2}$]
T	temperature [K]
$\mathbf{U}$	velocity vector [m s^{-1}]
w	wighting function
x_i, y_i, z_i	cartesian coordinated [m]

Greek symbols

μ	dynamic viscosity [kg m^{-1} s^{-1}]
ρ	density [kgm^{-3}]
θ	bias
$\mathbf{\Pi}$	Reynolds stress tensor [kg m^{-1} s^{-2}]
$\boldsymbol{\delta}$	Model constant
$\boldsymbol{\lambda}$	Model constant
$\boldsymbol{\tau}$	stress tensor [kg m^{-1} s^{-2}]

Sub and superscripts

ave	average
ci	cold side inlet
cf	cell face
fl	fluid domain
h	hot side
hi	inlet of the hot stream
loc	local value
nw	near wall
ref	refrence values
sl	solid domain
t	turbulent
w	wall
x, y and z	Dimension of the 3D cartesian coordinate system

Abbreviations

ACO	Ant-colony optimization
ANN	Artificial neural netwrok
CEL	CFX expression language
CFD	Computational fluid dynamics
DB	Dittus – Boelter
DNN	Deep neural networ
DNN-GA	Deep neural nework-Genetic algorithm

DT	decision tree
GA	genetic algorithm
kNN	k-nearest neighbors
LTR	low – temperature reservoir
GBM	gradient boost machine
LGBM	Light gradient booting mahcine
MOGA	multiobjective genetic algorithm
Mas	memetic algorithms
ML	Machine learning
PCHE	printed circuit heat exchangers
PDF	probability density function
PEC	performance evaluation criteria
PSO	Particle Swan Optimization
RANS	Reynolds – averaged Navier–Stokes equations
RF	random forest
RVFL	random vector function link
RSM	response surface methodology
RMSE	root mean square error
RGP	real gas properties
sCO_2	supercritical carbon dioxide
$sCO_2 - BC$	supercritical carbon dioxide Brayton cycle
SMO	social media optimization
SVM	support vector machine
SVR	support vector regression
WLS	Weighted Least Square
XGBoost	eXtreme Gradient Boosting

Introduction

Worldwide energy sectors are continuously working towards developing and improving technologies to produce clean and more efficient energy generation systems to fulfil the constantly increasing per capita demands. Concurrently, the interest falls on the sCO2 Brayton cycle ($sCO_2 - BC$), to construct a highly efficient thermodynamic cycle. sCO_2 fluids have high thermodynamic properties, compactness, safety, and low emissions, which makes a sCO_2 Brayton cycle superior to other thermodynamic cycles. In the Brayton cycle, after gaining heat from the source, the working fluid enters the turbine at a very high temperature, which significantly helps achieve the energy system's overall high efficiency [1]. The sCO2 Brayton cycle has been adopted in several industries and energy applications such as the petroleum industry, power generation, extraction processes, concentrating solar systems, fossil fuels, nuclear power, geothermal power, and waste heat recovery [2,3]. Numerous studies show that the overall performance of the Brayton cycle depends on several components and is very sensitive to the design and operating parameters. Therefore, optimizing the design and operating parameters dependency will help to predict the spirited performance of systems [4,5]. The advantages of the sCO_2 cycle can be further enhanced by replacing the shell and tube heat exchanger with a compact heat exchanger [6,7].

1.1. Printed circuit heat exchangers

Over the last decades, PCHEs have been widely proposed and are a clear choice for the supercritical Brayton cycle based on excellent heat transfer characteristics, high compactness, high effectiveness, and ability to withstand high pressures and temperature [8,9]. Abundant studies (experimental and numerical) have been carried out on PCHEs with different geometry designs. The zigzag channel configuration and semicircular cross-section are the most common configurations. They are widely used for better thermal characteristics, higher compactness, and ease of manufacturing than straight channels [10]. Furthermore, the S-shaped fins replaced the conventional zigzag channel geometry to change the flow directions. As a result, the recirculation and separation zones can be avoided, and it helps to enhance the hydrodynamic performance significantly in the context of the zigzag channel [11]. In this framework, Chu et al. [12], experimentally investigated the PCHEs with a zigzag channel under the SCO_2-water loop and proposed heat transfer and pressure drop correlations for the operation in the pseudo-critical region. They observed that Nusselt numbers and friction factors averagely decrease at certain operating pressure ranges as the zigzag angle increases from 15° to 25°. Similar studies have been carried out by Jeon et al. [13] for heterogeneous type PCHE. They conducted a sensitivity analysis on different channel geometries like; varying channel sizes, spacing, and cross-sectional shape of the heat source and heat sink channels. They found that the thermal hydraulic performance of the heterogeneous type PCHE is monotonically affected concerning incrementing in channel size. Lee et al. [14] also studied the different geometry configuration PCHE through the 3D-Reynolds-averaged Navier–Stokes (RANS) numerical method coupled with MOGA to enhance the performance and two-design parametric (effectiveness and non-dimensional pressure drop) effect of the PCHEs. They concluded that the effectiveness and friction factors of the PCHEs are interrelated and maximized performance can be obtained by keeping the zigzag angle the same on both hot and code sides. Figley et al. [15]

numerically investigated that the critical Reynolds number is higher during flow transition from laminar to laminar-to-turbulent in the semicircular channel than in a circular channel geometry PCHEs at high-temperature reactors. Therefore, they recommended that to obtain a better understanding of the effects of the channel geometry on the thermal hydraulic performance, the Reynolds number has to be considered as a critical parameter. Similarly, Kim et al. [16] studied different flow profiles (cross, parallel, and counterflow) in PCHEs and proposed a mathematical correlation for the thermal performance. The effectiveness of the PCHEs has been considered a critical function of geometrical parameters. Similarly, Li et al. [17] defined a new dimensionless factor called "working point," which considers the effects of working temperature and pressure. This method is proposed to evaluate the overall heat transfer performance of PCHEs on supercritical CO_2, and later they used it to validate with a double pipe heat exchanger system. Rao et al. [18] developed a thermo-economic model. They performed a multi-objective optimization on the design parameters for the Brayton cycle with the S-shaped fin printed circuit recuperator (PCR). They concluded that, compared to the mass fluxes, the recuperator's enthalpy efficiencies and recompression fraction play crucial roles in the optimization. They recommended multi-objective optimization to obtain better insight into the PCR design in the sCO2 recompression cycle. Tang et al. [19] studied the effect of axial heat conduction on the thermal performance of the zigzag PCHE at different Reynolds numbers (*Re*), where the effect was high at low *Re*. The thermal performance was found to be improved at lower thermal conductivity and mass flux, owing to axial heat conduction in the separation wall. Huang et al. [20] summarized the in-depth review on the numerical and experimental methods on thermal-hydraulic performance, including the different structures and different working fluids in PCHEs. They stated that to perform numerical simulations and obtain more accurate results than experimental, operating, and boundary conditions, turbulent models, geometric parameters, and structures should play a crucial role in investigating the overall performance of PCHEs, especially for the sCO_2 Brayton cycle.

While concluding the distinct aspects of the survey mentioned above, several studies have reported using different geometries like S-shaped fins and air-foil fins instead of zigzag channels. These changes in geometries have been reported to show significant improvement in hydro-thermal performance (due to reduced pressure drop). Henceforth, optimizing the design and operating parameters dependency will help to predict the enhanced performance of PCHE using a supercritical CO_2 Brayton cycles system. The subsequent sections briefly discuss the adopted method to optimize the PCHE channel geometry.

1.2. Machine learning methods

In the current scenario, Machine Learning (ML) techniques are progressively popular and executed in hydro-thermal analysis to obtain the optimum solutions with significantly less computing cost and time. An excellent application of ML is found with computational fluid dynamics (CFD), which has been highly advanced during the last few decades. It's the accuracy of operation. It is sensitive to the mesh, increasing complexity and computational requirements at multi-physics levels. Machine learning shows extraordinary potential to predict optimal solutions for complex multi-physics problems in this context. Behman et al. [21] used four different ML algorithms, namely, Support Vector Regression (SVR), Artificial Neural Network (ANN), Random Forest (RF), and Decision Tree (DT), are executed to obtain the heat transfer characteristics for the small-scale evaporative condenser. They concluded that SVM is most efficient in predicting heat transfer rate for small dataset sizes compared to other networks. The networks mentioned above and Multiple Linear Regression (MLR) were used to predict the fluid temperatures for a heat exchanger, Wherein ANN shows impressive results [22]. Huang et al. [23] used SVM to establish the data processing on experimentally collected data to predict the Nusselt number (*Nu*) for a heat exchanger in cryocoolers with cryogenic oscillating-flow conditions. Predictions had maximum error of 12.4% and R2 = 0.992. Likewise, to predict air injection effects in shell and tube heat exchanger, SVM, Random Vector Functional Link (RVFL), Social Media Optimization (SMO), and k-nearest neighbors (kNN), Machine learning algorithms are executed. Detailed analysis revealed that RVFL had more capability than others [24]. Gradient Boosting Machine (GBM) was used to predict refrigerant two-phase frictional pressure gradient inside brazed heat exchangers. The model reproduced the data with a mean absolute percentage error of 6.6% [25]. ANN, RF, AdaBoost, and Extreme Gradient Boosting (XGBoost) were executed to obtain the optimum heat transfer coefficients value in condensation mini/micro-channels. The comparison revealed that ANN and XGBoost had the best performance, with 6.8% and 9.1% MAE, respectively [26]. The off-design performance of the sCO2 turbine based on field reconstruction was predicted using the deep learning algorithm Convolutional Neural Network (CNN). Predictions of CNN had a relative error range of −5%–5% and had better performance than the five machine learning algorithms used before [27]. A Deep Neural Network (DNN) was proposed [28] to create a sCO2 turbomachinery off-design model. Results showed 101 to 104 better percent of MAE and Mean-Squared-Error (MSE) [29]. It can be inferred from above the main difference between all techniques is how accurate the solution can be for complex problems with a high number of variables and time to reach the optimum solutions. The added complexity over the GAs in the algorithms, as in MAs, PSO, ACO, and SFL, is essential for large problems that might take GAs much time to solve and improve their accuracy.

1.3. Research gaps and current study

The above literature review discussed in the introductions section indicates that it is deficient in research involving designing and optimizing the printed circuit heat exchangers (PCHEs) using efficient methods and channel geometries. At the same time, the enhancement in the PCHE designs can significantly improve the overall performance of the supercritical carbon dioxide cycle. The limited studies are available in the literature, such as the author's previous work [30] employed optimization procedures that entail gradient-free optimization methods. However, as an alternative to derivative-free optimization techniques, the deployment of gradient-based optimization techniques enables noticeably accurate results in an amount of time that is one order of magnitude smaller than that of derivative-free optimization algorithms [31]. Machine learning methods have been controlled to develop surrogate models that transcend the drawback of derivative-free optimization methods. Machine learning techniques enable approximated mathematical models of the nonlinear systems founded on sample data. The consequent models can suitably be employed for optimization problems, presenting an intrinsically continuous and differentiable correlation function that uses analytical gradient methods [32]. In this context, the current study involves a multilayered technique that utilizes CFD, machine learning techniques, and a multiobjective genetic algorithm to optimize C-shaped channel geometry for printed circuit heating exchanger for the first time author's best knowledge.

It should be noted here a previously proposed new channel geometry for PCHEs has been reoptimized (called; $optimze_{ML}$) by applying the above-mentioned multifaceted approach to 81 different geometries combinations. Three machine learning algorithms (section 3) are employed for the current study to be trained on numerical data (section 2). The ML algorithm with the best performance is chosen and coupled with the multiobjective genetic algorithm (MOGA) to optimize the design parameters. Finally, the thermo-hydraulic performance of the optimized C-shaped channel geometry ($optimze_{ML}$) is computed for a wide range of Reynolds numbers and compared with the PCHEs with zigzag channels and PCHEs with previously optimized C-shaped channels ($optimized_{RSM}$). The results suggest that PCHEs with $optimze_{ML}$ channel geometry showed almost 1.5 and 2.1 times improvement in thermohydraulic

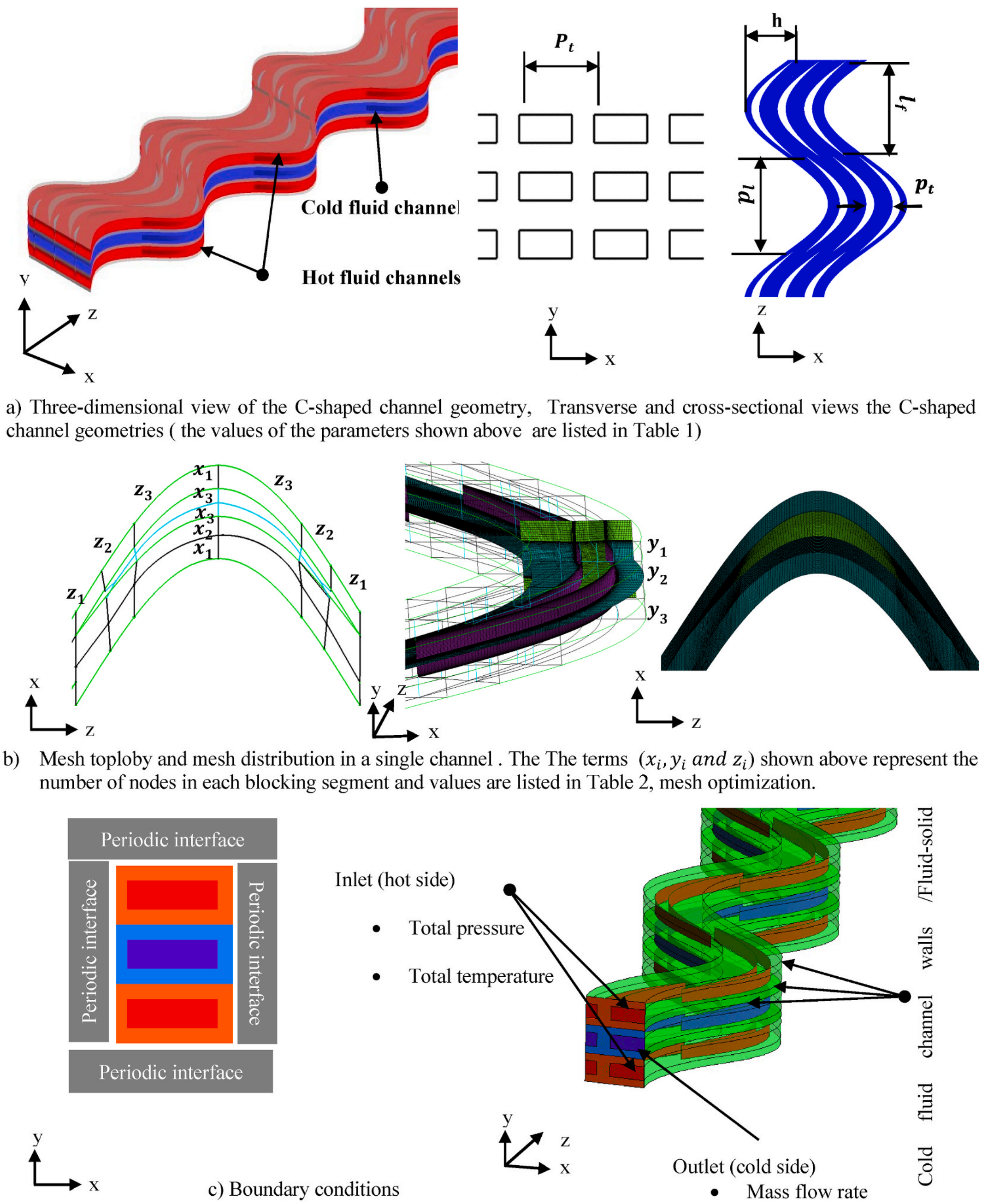

Fig. 1. a) Schematic diagram of proposed new channel geometries for the PCHE b) mesh topology and mesh distribution c) imposed boundary conditions.

performance compared to previously optimized ($optimze_{RMS}$) and base zigzag channel geometry, respectively.

2. Computational and mathematical modelling

In the present work, C-shape channel geometry has been reoptimized to enhance the thermo-dynamical characteristics of the PCHEs. To reoptimize the channel geometry (called $optimize^{ML}$), a deep neural network (machine learning algorithm) is trained on the CFD calculations for 81 different channel configurations (details ins section 2.1). The following computational model has been validated and adopted for the current study to compute the thermohydraulic performance of each configuration required to generate the training data.

2.1. Geometrical model

The geometry model of C-shape PCHE shows in Fig. 1 a [33], and corresponding design parameters values are presented in Table 1. In the proposed C-shaped fins geometry; fin length (l_f), fin depth (h), longitudinal pitch (p_l), transverse pitch (p_t), channel hydraulic diameter are proposed and used as a critical design parameters. C- shaped fins based on the sinusoidal curve were proposed [33] for smooth flow direction to avoid recirculation and separation zones. The sinusoidal fins have been placed in a staggered arrangement so that boundary conditions can be reinitialized after every fin pitch (longitudinal). More details on the proposed geometry can be found in previously reported work [33,34].

It is to be noted here that 81 geometry combinations (Appendix B) have been examined through CFD analysis, and data is used to train the ML model. In the previous study, only 31 proposed geometry combinations were reported [33].

2.2. Computational model

The physical models of the proposed fin geometries have been represented in mathematical terms using the steady form of the governing equations Eqs. (1)–(5). These equations have been numerically studied by commercial code ANSYS-CFX [35].

2.2.1. Steady state conservation equations

$$\nabla.\rho\mathbf{U} = 0. \tag{1}$$

$$\rho(\mathbf{U}.\nabla)\mathbf{U} = -\nabla p + \nabla.\boldsymbol{\tau} \tag{2}$$

$$\boldsymbol{\tau} = \mu\left(\nabla U + (\nabla U)^T - \frac{2}{3}\delta\nabla.\mathbf{U}\right) + \nabla.£ \tag{3}$$

In the ANSYS-CFX, $k-\varepsilon$ turbulence model [36–38] and Shear stress transport (SST) models are widely adopted to solve the boundary layer problems even under sharp pressure gradients. Several researchers chose the SST turbulence model [39,40]as it can get separation and recirculation zones accurately [41] that are much more likely to form within the PCHE [33,42]. Therefore, the SST turbulence model has been chosen to obtain the unknown Reynolds stresses (£) in the present analysis.

$$\nabla.(\rho\mathbf{U}H) = \nabla.\left(\frac{\lambda + \lambda_t}{C_p}\nabla h\right) \tag{4}$$

2.2.2. The equation for the solid domain

$$k_{sl}\nabla^2 T = 0 \tag{5}$$

2.3. Computational mesh

The computation mesh was constructed based on the parameter values of each geometrical configuration through ANSYS ICEM-CFD. The SST turbulence modelling conditions were satisfied by ensuring $y^+ < 1$ and keeping 15 nodes within the boundary layer thickness. A mesh optimization study was conducted using four meshes, A, B, C, and D. details of these four meshes are shown in Table 2, while the parameters listed in the Table are displayed in Fig. 1b. Mesh C was finalized based on less computational cost as the difference in the Nusselt number values computed using meshes C and D is very small. Further details on the mesh optimization study can be found in the author's previous work [33].

Table 1
Design parametric of channel geometry.

Plate material	SS316L
Pitch along length (p_l)[mm]	9.0
pitch in transverse direction (p_t)[mm]	2.35
Length of the channel (l_f)[mm]	7.24
Fin angle (θ)[degree]	40^0
Transverse depth of the channels (h)[mm]	3.03
Hydraulic diameter (D_h)[mm]	1.106
Plate thickness (P_t)[mm]	1.63

Table 2
Mesh finalization.

	x1	x2	x3	y1	y2	y3	z1	z2	z3	Nodal count	CPU time/iteration[s]	Nusselt number
M1	10	12	18	7	20	5	8	10	12	0.8 M	5	35.7
M2	20	25	25	10	30	10	15	18	25	4.3 M	42	51.8
M3	25	35	35	15	40	15	25	25	30	11.2 M	95	53.9
M4	30	40	40	20	40	20	30	30	35	17.5 M	205	53.4

2.4. Boundary conditions and model validation

A full-length (896 mm) heat exchanger as one cold between two hot channels has been modelled, as shown in Fig. 1c. At inlet, pressure, and temperature, the mass flow rate at the outlet is kept fixed. As mentioned above, high computation time and resources are needed to simulate the whole geometry. Therefore, in the present analysis, the periodic boundary conditions have been adopted, which helps to study the reduced number of channel geometry and significantly reduces the computational efforts without compromising the accuracy of the solution. The boundary conditions imposed at interfaced shown in Fig. 3 are articulated employing Eq. (6), where the external walls of the PCHEs are considered adiabatic.

$$\left.\begin{aligned} &U = 0 \\ &T_{sl} = T_{fl} \\ &k_{sl}\frac{\partial T_{sl}}{\partial n} = k_{fl}\frac{\partial T_{fl}}{\partial n} \end{aligned}\right\} \tag{6}$$

2.5. Validation of the computational model

Validation of the computational model is conducted using zigzag channel geometry; further details on the validation can be found in the author's previous work [33,43]. It is to be noted here that validation of the model is conducted using the full length of the channel, i.e., 892 mm, used by Ishizuka [44,45] due to the unavailability of the experimental data for smaller channel lengths. Boundary conditions used to validate the computational model are listed in Table 3 (set A). The comparison of the experimental and numerical values is listed in Table 4 for the full-scale model. The comparison suggests that the computed values from the employed model are in close agreement with the experimental values.

It is shown in the author's previous work [45] that the computational model using shorter channel lengths can be used to mimic the thermohydraulic characteristics of the full-scale models at much reduced computational costs. Hence, for the current study, a shorter channel length (100 mm) is used for both channel configurations instead of the full length of the channel to reduce the computational cost. Hence, imposed boundary conditions are displayed in Table 3 (set B) that are extracted from the temperature and pressure profiles computed from the full-length simulations of PCHE [43] shown in Fig. 2. It is to be noted here mass flow rate conditions are imposed at both outlets of the hot and cold fluid channels in terms of Reynolds number. Reynolds number on the cold side is always double the Reynolds number on the hot side as the configuration of PCHE is such that a cold channel is sandwiched between the two hot channels to avoid higher pressure losses on the hot side [46].

2.6. Post-processing

To evaluate the overall performance of PCHE, the local heat transfer coefficient (h_{loc}), Nusselt number, Average Nusselt number ($\overline{Nu}$), local (f_{loc}) and average friction factor (f_{ave}) values are calculated as follows,

$$h_{loc} = \frac{q_{cf}}{T_w - T_{nw}} \tag{7}$$

Table 3
Listed boundary conditions used to validate the present model.

	Conditions		values
Set A Channel length 890 mm	Hot side	P_{hi}[kPa]	2545.5
		T_{hi}[oC]	279.9
		m_h[kg s^{-1}]	0.0001445
	Cold side	P_{ci}[kPa]	8353.22
		T_{ci}[oC]	107.9
		m_C[kg s^{-1}]	0.0003152
Set B Channel length 100 mm	Hot side	P_{hi}[kPa]	2545.5
		T_{hi}[oC]	279.9
		Re_h[kg s^{-1}]	15000 (for various configurations of C-shaped channel) 2500-30000 (For otptimzed geometry)
	Cold side	P_{ci}[kPa]	8288
		T_{ci}[oC]	205
		Re_C[kg s^{-1}]	30000 (for various configurations of C-shaped channel) 5000-60000 (For otptimzed geometry)

Table 4
Comparison of the obtained numerical data with experimental data [44,45].

	Numerical results	Experimental results	% Difference
Pressure drop hot-side [Pa]	25490	24180	3.58
Pressure drop cold-side [Pa]	75859	73220	3.6
Temperature difference hot-side [oC]	169.20	165.46	2.26
Temperature difference cold-side [oC]	142.90	141.1	1.28

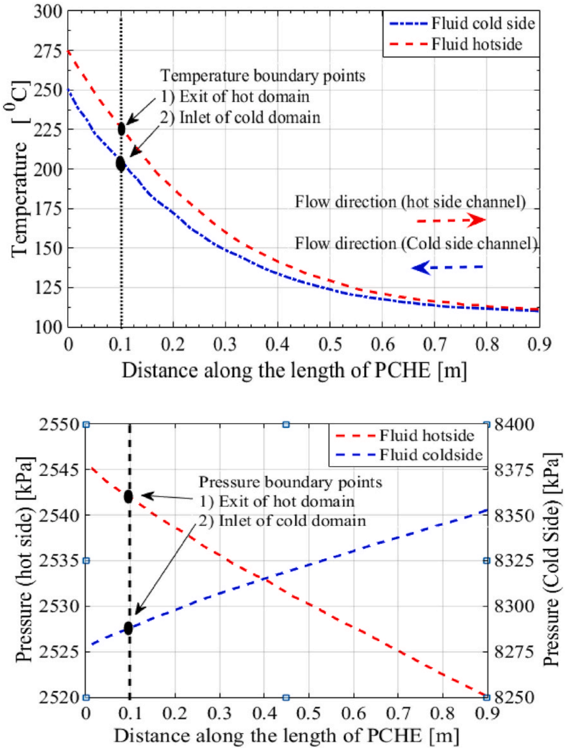

Fig. 2. Distribution of the temperature and pressure profiles for a full length of the PCHE [45].

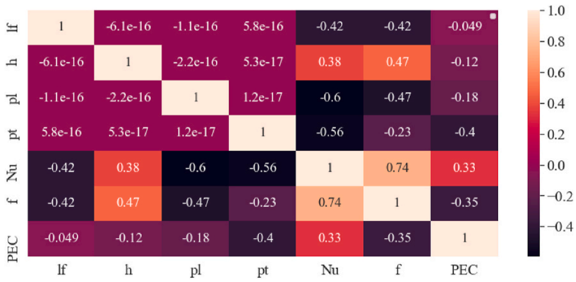

Fig. 3. Heat map showing the sensitivity of each one of the parameters to the variation in output variables.

$$Nu_{loc} = \frac{h_{loc} D_h}{k_{loc}} \tag{8}$$

$$\overline{Nu} = \frac{1}{n} \sum_{i=1}^{n} Nu_i \tag{9}$$

$$f_{loc} = \frac{dp}{dz} \cdot \frac{2}{\rho_{loc} U^2} \cdot D_h \tag{10}$$

$$f_{ave} = \frac{1}{n} \sum_{i=1}^{n} f_i \tag{11}$$

The f_{loc} is calculated at the midpoint through the channel in the direction of flow. The important geometrical parameters used to characterize the C-shaped channel are provided in Appendix B alongside the computed outputs. The first four columns are the length of the header of the channel (l_f), transverse depth of the channel (h), longitudinal pitch (p_l), and transverse pitch (p_t). These four parameters are the inputs where all the given dimensions are in mm. The output parameters are Nusselt number (Nu) and friction factor (f). From the output parameters, a performance evaluation criterion (PEC) is calculated to provide a single parameter to evaluate the overall performance of the heat exchanger using the following equation: The below definition of the PEC is adopted from the literature [47,48].

$$PEC = \frac{\frac{\overline{Nu_i}}{\overline{Nu_{ref}}}}{\left(\frac{f_{ave,i}}{f_{ave,ref}}\right)^{\frac{1}{3}}} \tag{12}$$

3. Optimization methodology

Once the required data is computed, the optimization methodology adopted in the current work has been described in the current section. The sensitivity analysis of the calculated data is first performed (section 3.1) to identify the sensitivity of the input parameters. Later, the data is used to train three machine learning models, i.e., Deep Neural Network, XGBoost, and LGBM algorithm. The best algorithm is chosen based on its prediction performance and required computational costs (section 3.2). Lastly, the finalized ML model is coupled with the multi-objective genetic algorithm to optimize the design parameter Section 3.3).

3.1. Sensitivity analysis

The sensitivity analysis has been performed using the Weighted Least Square (WLS) method. Fig. 3 shows the heat map for the sensitivity and dependency from input to output parameters. Accordingly, the sensitivity of one input parameter to the variation in the other three is nearly zero since they are independent variables. A higher value indicates higher sensitivity of the parameters in the column to the variation in the parameters in the row. On the other hand, the positive and negative signs indicate whether the output quantities trends due to input parameters are direct or inverse. It is found that both output parameters Nu and f are sensitive to all opted input parameters. It is found that the sensitivity of Nu to p_l and p_t is nearly identical and highest among all input parameters. At the same time, f is most sensitive to h and least sensitive p_t.

3.2. Training of the machine learning model

Three machine learning, i.e., DNN, XGBoost, and LGBM, are used in the current work to train the data, and the best model based on the prediction accuracy and computational cost is finalized. The study adopted model details are provided in the following subsections.

3.2.1. Deep neural network

The frequently used feed forward – backpropagation architecture of DNN, also known as Recurrent Neural Network (RNN), was utilized to develop a systematic model with geometrical components as input and yield of thermal and hydraulic quantities output to the model. In this design, data flow forward and backwards,i.e., from the input layer to the output layer and vice versa. Weights are the parameters connected with the assembly of two neurons and are adjusted during the training process controlled by the optimizing algorithms. The input layers consist of the neurons equal to the input number of variables containing the scaled data. The data to the next layer is fed from the previous layer that accounts for the weighted sum of all the neurons values by adding bias (θ) values, as displayed in the equation below.

$$\mathrm{x} = \sum_{i=1}^{n} x_i w_i + \theta \tag{13}$$

It is to be noted here that the data values to the next layer first pass through the activation function (e.g., linear, RELU, sigmoid etc.).; the data received by the next layer from the previous layer is expressed in Eq. (14).

$$y = activation\ function\ (x) \tag{14}$$

The frequently utilized error function, the root-mean-squared-error (RMSE) castoff in this work, is described as:

$$\mathrm{RMSE} = \sqrt{\frac{\sum_{i=1}^{N} \sum_{j=1}^{M} \left(y_j^i - \hat{y}_j^i\right)^2}{NM}} \tag{15}$$

where N is the number of patterns used in training; M is the number of output nodes; i denotes the index of the input pattern (vector) and y_j^i and $\hat{y}_j^i$ are the target and predicted outputs of the nth output node, respectively. The RMSE is minimized using the error back-propagation (EBP) algorithm [49], which uses the gradient descent technique. Before starting the DNN architecture optimization, the input and output data are normalized to get a good distribution over the data range. Input data are normalized from 0 to 1, while output data is by the logarithmic function since friction values are more concentrated on one side of the range than the other.

Once the nonlinear DNN model generalization is finalized, its geometrical input design variables l_f, h, p_l andp_t are optimized to improve the system and increase the efficiency of the C-shaped PCHE. The conventional optimization of a single variable at a time approach is time-consuming and ignores the combined interaction effects between the different factors in nonlinear systems. Therefore evolutionary stochastic searching methods that can solve complex optimization problems should be used [50].

3.2.2. XGBoost algorithm

XGBoost is a boosting algorithm that uses supervised learning based on gradient boosting trees. It integrates predictions of a "weak" decision tree model to achieve a "strong" one via training processes. It can avoid over-fitting by adding a regularization term, and parallel computing makes learning faster. As the number of trees increases, the loss function decreases; therefore, the loss is minimum at the last tree. The final tree model for (t) trees can be obtained by Ref. [51]:

$$\hat{y}_i^{(t)} = \sum_{k=1}^{t} f_k(x_i) = \hat{y}_i^{(t-1)} + f_t(x_i), \tag{16}$$

where $\hat{y}_i^{(t)}$ is the final tree model, $\hat{y}_i^{(t-1)}$ is the previously produced model, $f_t(x_i)$ is the newly created model, and t is the total number of base tree models. The target of this algorithm is to find a classifier that minimizes the target loss function (Obj), which is given as [51]:

$$Obj^{(t)} = \sum_{i=1}^{t} L\left(y_i, \hat{y}_i^{(t)}\right) + \sum_{i=1}^{t} \Omega(f_i), \tag{17}$$

where y_i is the actual value, $\hat{y}_i^{(t)}$ is the predicted one, and $\Omega(f_i)$ is a regularization term, which is given as [51]:

$$\Omega(f) = \gamma T + \frac{1}{2}\lambda\omega^2, \tag{18}$$

where T is the number of leaves; ω is their weight; λ and γ are coefficients, with default values set as $\lambda = 1, \gamma = 0$. Substituting Eqs. (17) and (18) gives (with some steps can be found in Ref. [52]):

$$Obj^{(t)} = \sum_{i=1}^{t} L\left(y_i, \hat{y}_i^{(t-1)} + f_t(x_i)\right) + \Omega(f_i) + constant \tag{19}$$

Eq (17) again can be rewritten as [51]:

$$Obj^{(t)} = \sum_{i=1}^{t} \left[g_i f_t(x_i) + \frac{1}{2} h_i f_t^2(x_i) \right] + \Omega(f_i), \tag{20}$$

where g_i and h_i are the first and second-order gradient statistics on the loss function, respectively.

The XGBoost can be used in Python 3.7, where the most important hyperparameters are the number of trees and the depth of the tree.

3.2.3. LGBM Algorithm

LGBM is another machine learning algorithm based on gradient boosting decision trees. This algorithm is similar to XGBoost since it is a boosting algorithm, but its decision trees are updated based leaf-wise, while the XGBoost trees are updated based level-wise. More details about the difference between leaf and level-wise trees can be found in Ref. [53]. Three steps can briefly summarize the algorithm; the first step is to initialize the weak learner [53]:

$$f_0(x) = \text{argmin}\left(\sum_{i=1}^{n} L(y_i, c)\right), \tag{21}$$

where $f_0(x)$ is a weak learner, $L(y_i, c)$ is the loss function, and n is the number of samples. The second step is to calculate the negative gradient of the loss function to obtain a new tree, $f_1(x)$. For tree m and J leaf nodes, the stronger tree is updated as [53]:

$$f_m(x) = f_{m-1}(x) + \sum_{j=1}^{J} c_{mj} I\left(x \in R_{mj}\right), \tag{22}$$

where I is an indicator function, and its value is one if $x \in R_{mj}$ otherwise, it is zero, R_{mj} is leaf node area, and c_{mj} is a parameter given for $i = (1, 2, \ldots .M)$ as:

$$c_{mj} = \text{argmin}\left(\sum_{x \in R_{mj}} L(y_i, f_{m-1}(x_i + c))\right) \tag{23}$$

The third and final step is to obtain the last regression tree for M trees [53]:

$$F(x) = \sum_{m=1}^{M} \sum_{j=1}^{J} c_{mj} I\left(x \in R_{mj}\right) \tag{24}$$

LGBM is also included in Python 3.7, and the hyperparameters are similar to that of XGBoost.

3.3. Multi-objective genetic algorithm (MOGA)

Once the nonlinear ML model and its generalization are finalized, the geometrical input variables are optimized to improve the system and increase the efficiency of the C-shaped PCHE. The conventional optimization of a single variable at a time approach is time-consuming and ignores the combined interaction effects between the different factors in nonlinear systems. Therefore evolutionary stochastic searching methods that can solve complex optimization problems should be used [50]. Almost all of the techniques are based on mimicking the natural biological behaviour of species. The first technique is the genetic algorithms (GAs) [54]; this method is developed based on the biological systems of improved fitness of the living species and evolution through reproduction. Due to its success and ability to reach optimum solutions for problems with large amounts of variables, it has been used in applications in science and engineering [55–57]. GAs optimization goes through four different stages to find a solution to a given problem. It begins with an initialization of a random population of solutions, often called (chromosomes); afterwards, each chromosome combination fitness is evaluated against an objective function, which indicates the selection of best chromosomes, genetic propagation, and survival of selected parent chromosomes using crossover and mutation to exchange information and create the new population of chromosomes. The new population is evaluated, and if they provide better solutions than weak population members, the whole process continues until a suitable result is achieved. The best fit evolves after repeating the loop until convergence forms the problem's near-optimum solution [55]. The main parameters used in a GA algorithm are population size, number of generations, crossover rate, and mutation rate.

In addition to the GAs algorithms, there are four other optimization techniques. The memetic algorithms (MAs) [58] are similar to GAs with a small naming difference of the chromosome called memes. The main difference between those techniques is that MAs allow all the chromosomes and parent chromosomes to gain experience using a local search before getting involved in the evolution process. MAs use the same four steps in GAs with an addition of a local search mechanism. It begins with creating the initial random population; then, on each member of the population, a local search is performed to improve its experience and obtain a population with local optimum solutions. After going through the rest of the steps, the new population members are subjected to the local search, and the whole process continues until a suitable result is achieved. The main parameters used in MAs are similar to GAs with an additional local search mechanism.

Particle swarm optimization (PSO) [59] is an optimization technique inspired by the social behaviour of a flock of migrating birds trying to reach an unknown destination. In PSO, each solution is a bird in the flock; the bird here is analogous to a population member (chromosome) in GA. In contrast to GA, the PSO evolutionary process doesn't depend on creating new birds from parents. The evolution of the birds depends on their social behaviour and movement towards a targeted destination. The PSO different steps to find a converged solution start with each bird in a flock of birds that communicate together by looking in a specific direction; after communicating together, they indicate the bird with the best location. Each bird adjusts its velocity towards the best bird from its located position. The whole process repeats from the new locations until the flock of birds reaches its desired destination. The main parameters used in PSO are the number of birds, number of generation cycles, the maximum change of a bird's velocity, and a balancing parameter between the global search of destination and local search of a best-located bird.

Ant-colony optimization (ACO) [60] is another technique similar to PSO in that they evolve using their social behaviour instead of genetics. This method was developed based on how ants can find the shortest path over obstacles between their nest and meal. Biologically, ants depose pheromone trails whenever they walk, which is an indirect communication between the ants. This method initially starts with ants leaving their nest to search for meals; they move randomly over different obstacles in searching for food while deposing the pheromone. After finding their meal, ants carry it to the nest and return, following their pheromone trails. As time goes by, the pheromone over the short path will be more than the other paths; since it is shorter, more ants will travel and depose the pheromone over it. New ants will start moving from the nest to find their meal and choose the shortest path due to the high pheromone levels. Over time all ants will choose the shorter path due to the same reason [61]. The main parameters used in ACO are the number of ants, number of iterations, pheromone evaporation rate, and pheromone reward factors.

The last optimization technique is the shuffled frog leaping algorithm (SFL) [62] which combines the benefits of the genetic and social behaviour techniques. In this method, the population contains frogs separated into subsets of groups called memeplexes, and they have different cultures of frogs that perform local searches. Individual frogs within each group can hold their ideas. The other frogs can influence these ideas and evolve through a memetic process; after some evolutions, the ideas are passed among the groups in a shuffling operation. The local search and shuffling process continues until a defined convergence forms the optimum solution. The main parameters used in SFL are the number of frogs, the number of memeplexes (groups), generations for each group before shuffling, shuffling iterations, and the maximum step size of the frog.

The main difference between all techniques is how accurate the solution can be for complex problems with high variables and time to reach the optimum solutions. The added complexity over the GAs in the algorithms as in MAs, PSO, ACO, and SFL are essential for large problems that might take GAs much time to solve and improve their accuracy [50]. However, there are only four output variables in the C-shaped channel design. For such small optimization problems, all of the above techniques perform well in a reasonable amount of time. Therefore, only GA will be used as an optimizing technique due to its simplicity and accuracy for small problems.

For the following problem set of data, a population size of 100 is defined, and the crossover and mutation fraction is taken as 0.8

and 0.2, respectively. In each iteration, 95% of the new population is generated through mutation and crossover of the previous population. At the same time, the remaining 5% is the upper elite of the prior population that comes as it is in the new population. Fitness evaluation was carried out based on the average changes in the fitness function. Convergence tolerance is taken to be 10^{-6} for both function tolerance and constraint tolerance. The schematic of the optimization process is shown in Fig. 4.

4. Results and discussions

Current work deals with reoptimizing the PCHEs with C-shaped channel geometry maximizing its thermohydraulic characteristics. For the optimization process, four design parameters, i.e., the length of the channel (l_f), transverse depth of the channel (h), longitudinal pitch (p_l) and transverse pitch of the channel (p_t). The ranges of the design variable used for the current work are listed in Table 5. The authors [33] optimized the same channel geometry using response surface methodology and data generated from 27 different channel designs bounded by the design parameters listed in Table 5. However, the current study has utilized Machine learning technology coupled with the multi-objective genetic algorithm (MOGA). Thermohydraulic performance data is computed employing the 3D-RANS model for 81 different designs of the C-shaped channel bounded by the design parameters and their ranges listed in Table 5. Boundary conditions used for these simulations are listed in Table 3 as set B. It is to be noted here the fixed value of the Reynolds number on both hot and cold sides, i.e., 15000 and 30,000, respectively. The chosen Reynolds number is based on the author's previous work [6] where it is recommended for the compact designs of the heat exchanger and supervisor overall performance of the sCO2-BC.

It is to be The generated date is used to train the three different ML models, i.e., DNN, XGBoost, and LGBM algorithm. The prediction accuracy of all the trained models is then compared, and the model with the highest accuracy is selected for further predictions. Once the best ML model is identified, the trained ML model is used as a fitness function to predict the thermohydraulic characteristics of the various designs of C-shaped channel geometries during the optimization process utilizing the multi-objective genetic algorithm (MOGA).

The performance comparison of different machine learning algorithms is provided in Section 4.1; the trends of the thermohydraulic characteristics predicted by the deep neural network are discussed in 4.2, and optimization of the C-shaped channel geometry (optimized$_{ML}$) along with its performance comparison with the zigzag and previously optimized C-shaped channel geometry optimized$_{RSM}$ are discussed in section 4.3.

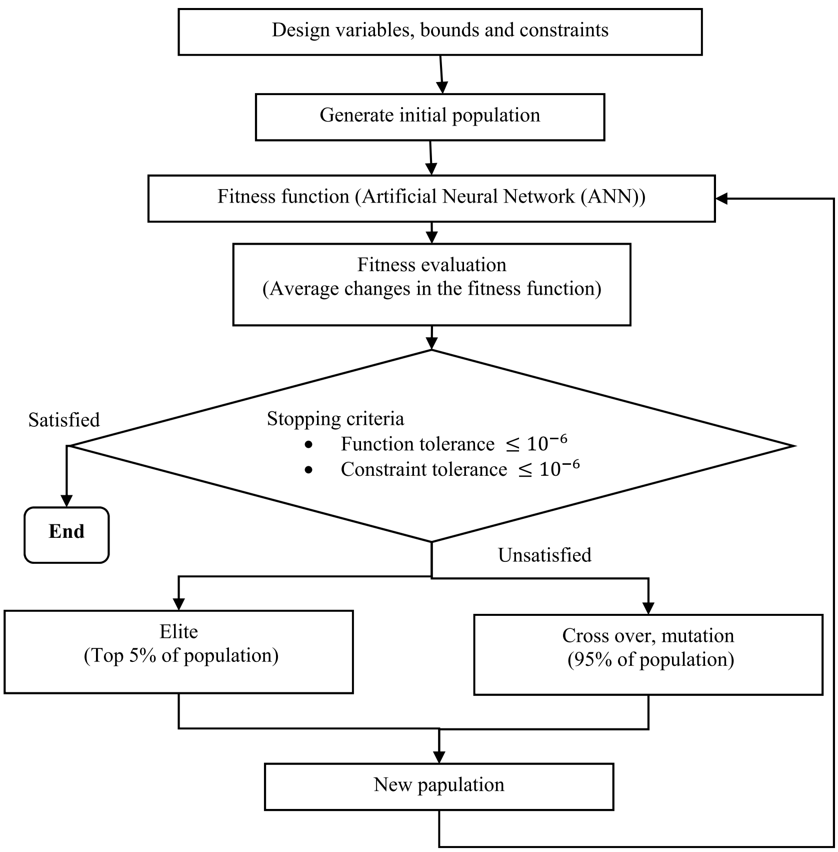

Fig. 4. Schematic genetic algorithm.

Table 5
Geometrical variables with their lower and upper bounds.

Geometrical variable		Lower and upper bounds
length of the channel (l_f) [mm]	x_1	1.81–5.43
Transverse depth of the channel (h) [mm]	x_2	1.515–4.545
Longitudinal pitch (p_l) [mm]	x_3	2.715–4.525
Transverse pitch (p_t) [mm]	x_4	1.7625–2.9375

4.1. Algorithms performance comparison and optimum model

4.1.1. Training of the DNN

The architecture of the optimized DNN is illustrated in Fig. 5a. It was found that for the given structured data set, a neural network with two hidden layers consisting of 4 and 3 neurons in the first and second layer, respectively, provides an optimized network for the prediction of both *Nu* and *f*. As discussed above, 81 geometry combination has been used to train the ML. In that, 85% of data was used for training, and the remaining 15% was preferred for testing. The professional network had 2.73% and 4.03% RMSE during the training and testing sets, respectively. As observed in Fig. 5b, the obtained regression (trained and tested data) representation agrees with the fitted line by the DNN for both *Nu* and *f*.

4.1.2. XGBoost results

In the XGBoost algorithm, three hyperparameters (number of trees, depth of the tree, and learning rate) were tuned, and the rest was left to the default values. The number of trees is 5000; increasing it to higher values increases the computational time without significantly enhancing the predicting performance. The depth of the tree is**1**, and rising it weakens the performance. Finally, the learning rate is 0.1, where changing it does not affect the performance. XGBoost has better performance in predicting *Nu* when it is compared with *f*. The average relative percent error for 17 validation data points is 2.3% for *Nu* and 3.8% for *f*. Fig. 5c shows the predicted *Nu*, and *f* vs. the true values using 20% for validation has better performance in comparison to the DNN-GA.

4.1.3. LGBM results

The predicted *Nu* and f by LGBM are shown in Fig. 5d. Again, the same hyperparameters used for XGBoost are tuned here for LGBM. The number of trees used is 5000, the depth of the trees is 1, and the learning rate is 0.15. Increasing the number of trees beyond 5000 has no effect on the performance with increasing computing time; improving the depth of the tree degrades the accuracy, and increasing or decreasing the learning has no effect on the accuracy. The average percent error of predicting *Nu* is 2.3%, while predicting f is less accurate with a 3.7% average percent error. Both XGBoost and LGBM have very similar prediction performance, as one can notice from Fig. 5c and d.

Table 6 shows the coefficient of determination for the three algorithms used. DNN has a slightly better R2 than XGBoost and LGBM, but all three models generally perform well. XGBoost and LGBM have very similar predictions, as in Fig. 5c and d, which is reflected in the equal values of R2 for both. DNN performs slightly better in predicting f than the other two models.

4.2. The trends of the thermohydraulic characteristics predicted by the deep neural network

The best model identified (DNN) is used to investigate the output parameters trends while varying the geometrical input parameters. Fig. 6a shows the variation of *Nu*, *f*, and PEC as a function of l_f and h while keeping p_l and pt as constants. It has been observed that *Nu* increases with increasing h and decreasing lf where the variation of *Nu* is approximately linear. The maximum value of *Nu* is located where h is maximum, and l_f is minimum. The surface of f, on the other hand, has a global minimum where increasing h amplifies f while increasing l_f decrease initially and then increase f slightly. The global minima are located where h is around 2.3 mm, and l_f is 4.5 mm. In contrast with f, PEC has a global maximum where the variation of both h and lf has almost the same effect on PEC. The global maxima are located where h is around 3 mm, and lf is around 3.6 mm.

Similarly, Fig. 6b shows the trend of *Nu*, f, and PEC as functions of pl and pt and constant h and l_f. Increasing pl and pt decrease *Nu* where the optima are located at minimum pl and pt. However, increasing pl and pt decreases f first, then raises it slightly. The minimum f region is at $pl = 3.6 - 4.1\ mm$, and $pt = 2.3 - 2.6\ mm$. In contrast, increasing pl and pt increases PEC first and then decreases it. The maximum value of PEC occurs in the region where $pl = 3.6 - 4.1\ mm$, and $pt = 2.3 - 2.6\ mm$. Finally, by comparing Fig. 6a and b, the output parameters are more sensitive to the variation of h and l_f compared to the variation of pl and. pt.

4.3. Optimization of the C-shaped channel geometry (optimized^{ML})

The DNN was chosen among the training algorithms based on the best performance, as discussed in section 4.1. Therefore, for the optimization of the C-shaped channel geometry, it was linked with the multi-objective genetic algorithm (MOGA). The list of design variables and their rages are listed in Table 5. Using the parameters for the GA discussed in section 3.3, it took the optimization algorithm 124 generations to converge, and the computed Pareto front is shown in Fig. 7. Compared with the provided data set, the hybrid DNN-GA produced an optimized geometry with a higher PEC than any given data set within a few minutes of computational work. This combined DNN-GA methodology is very useful during the optimizations stages of the geometrical aspect for different computational fluid dynamics applications since running over this huge range set of different design variables would consume an unrealistic amount of computational time. Therefore, more time and cost-efficient design optimization methods can be achieved by combining computational fluid dynamics with machine learning algorithms.

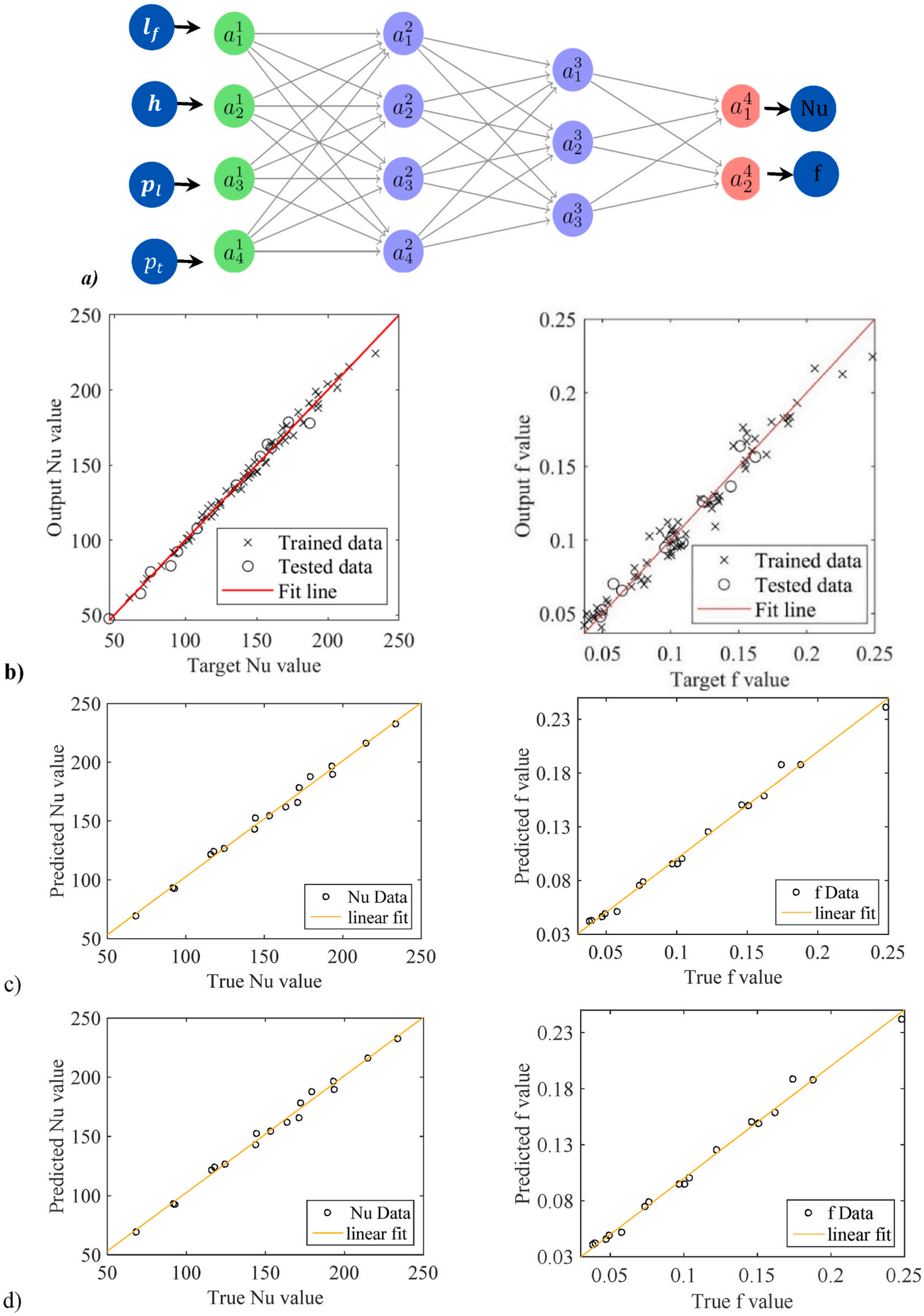

Fig. 5. a) Deep neural network, b) Predicted *Nu* vs true one (left) and predicted f vs true one (right) using DNN, c) Predicted *Nu* vs true one (left) and predicted f vs true one (right) using XGBoost, d) d)Predicted *Nu* vs true one (left) and predicted f vs true one (right) using LGM.

Table 6
The coefficient of determination for the three algorithms used.

Algorithm	R^2	
	Nu	*f*
DNN-GA	0.996	0.994
XGBoost	0.990	0.993
LGBM	0.990	0.993

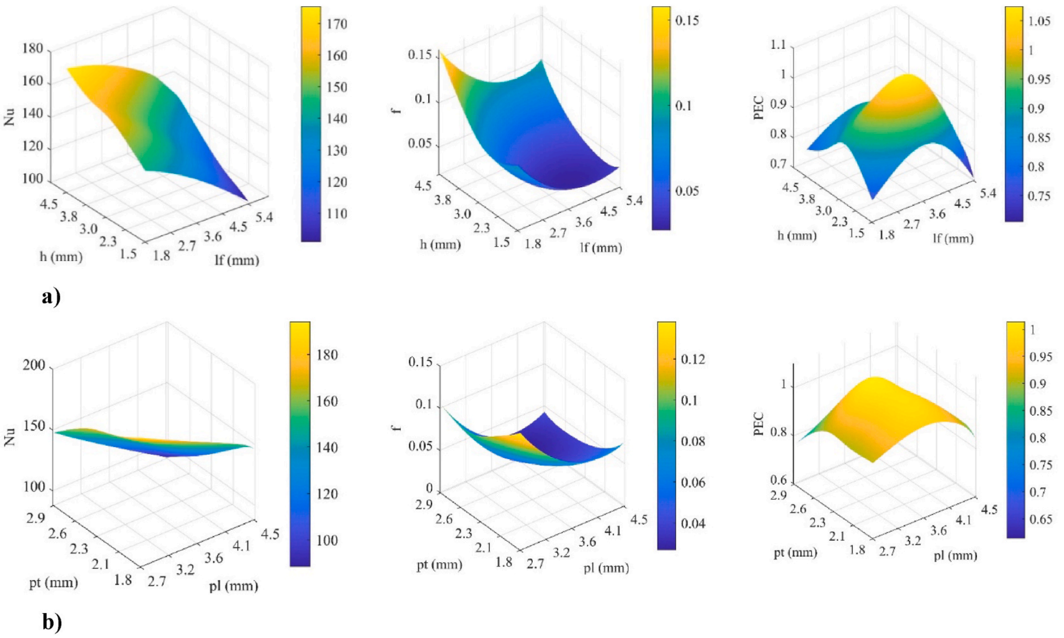

Fig. 6. a) The variation of *Nu*, *f*, and *PEC* with varying *h* while $p_l = 3.62$ mm and $p_t = 2.35$ mm, b) The variation of *Nu*, *f*, and (*PEC* with varying ***pl*** and ***pt*** and constant $\boldsymbol{h}$ = 3.03 mm and.$\boldsymbol{lf}$ = 3.615 ***mm***

Fig. 7 shows the Pareto front computed by coupling the trained deep neural network (DNN) with a multi-objective genetic algorithm (MOGA) displaying optimal geometries of the C-shaped channel geometries. Every point on the Pareto front represents an optimal solution where the improvement in an objective function can be achieved at the second cost. If the designer is interested in minimum values of the friction factor (*f*), region A will suit the desired condition. However, the values of the Nusselt number corresponding to the design of region A are minimum. At the same time, if one is interested in higher values of the heat transfer coefficient with no concern for *f* values, region C would be suitable under these conditions.

On the other hand, the overall performance of the heat exchanger is a critical factor in the design of the PCHEs. The size of the heat exchanger and the cycle's performance is highly dependent on the overall performance of the heat exchanger [6]. In this reference, to find a good compromise between the values of *Nu* and *f*, the performance evlatuation critereia (PEC) is used. The maximum values of the PEC corresponds to region B displayed in Fig. 7. The region B displaying Pareto fronts with friction factor values ranging from 0.04 to 0.06, Nusselt number values varying from 150 to 170 correspond to a maximum value of the PEC (1.09) and provide a reasonable compromise between the two objective functions.

4.4. Performance comparison of the optimized channel geometry under a wide range of conditions

The full list of the optimal designs forming the Pareto front (Fig. 7) is itemized as appendix C. At the same time, the selected geometries corresponding to regions A, B and C are listed in Fig. 7. As discussed above, the C-shaped channelled designs corresponding to region B provide a good compromise between *Nu* and f and exhibit the highest values of the PEC (overall performance evaluation criteria). Hence, a geometrical configuration lying in region B is used to investigate its performance under a wider range of the Reynolds number. i.e., $2500 < Re < 30,000$ (hot side), $5000 < Re < 60,000$ (cold side) using 3D RANS simulation. The validated computational model is presented in section 2 to evaluate the performance of the zigzag, base C-shaped channel geometry and optimized C-shaped channel geometry. The chosen optimized geometrical configuration is highlighted in Fig. 7. Later, the performance of the opted optimized channel geometry is compared with the conventional zigzag and previously optimized channel geometry employing response surface methodology using the limited data set.

Fig. 8a shows a comparison of the Nusselt number for the zigzag channel, C-shaped channel (base geometry), C-Shaped channel (optimized$_{RMS}$), and C-Shaped channel (optimized$_{ML}$). The confirm lines show the quantities on the cold side, and the dotted lines

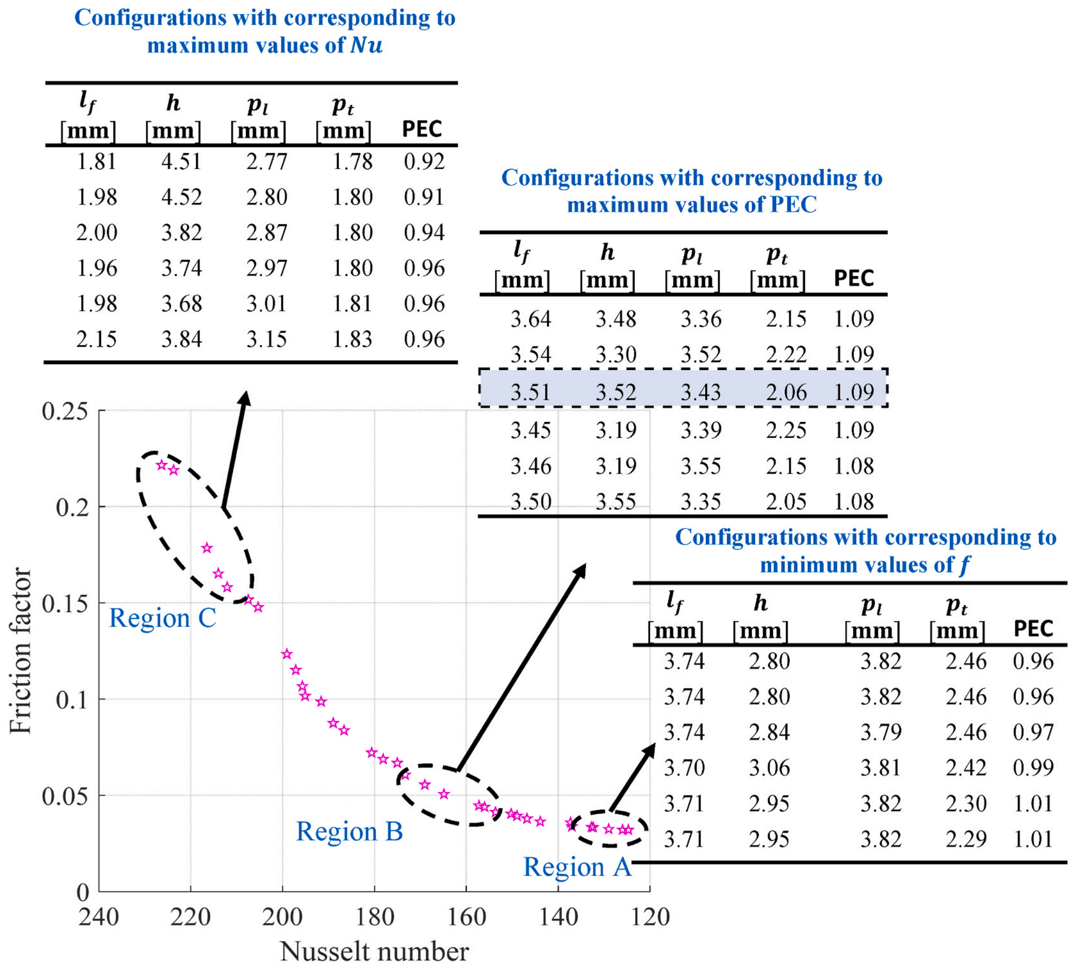

Fig. 7. Pareto front computed by coupling the trained deep neural network (DNN) with a multi-objective genetic algorithm (MOGA) showing optimal geometries of the C-shaped channel geometries.

represent the flow on the hot side. The comparison shows that the thermal performance for zigzag channel geometry is superior among all C-shaped base and optimized channel geometries. However, the highest thermal performance among the C-shaped channel geometries is found for the optimized$_{ML}$. Nusselt number for the optimized$_{ML}$ is found (8-20)% and (1-12)% higher than the base channel geometry and optimized$_{RMS}$ channel geometries, respectively, on the cold side. At the same time, the corresponding improvement for optimized$_{ML}$ is found (12–19)% and (2–9)% on the hot side while compared with the base channel and optimized$_{RMS}$ channel, respectively.

Fig. 8b shows a comparison of friction factor values for the zigzag channel, C-shaped channel (base geometry), C-Shaped channel (optimized$_{RMS}$), and C-Shaped channel (optimized$_{ML}$). The comparison demonstrates that the hydraulic performance for zigzag channel geometry is substantially poorer among all C-shaped channel geometries, i.e., C-shaped base, optimized $_{RMI,}$ and optimized$_{ML}$. Friction factor for the optimized$_{ML}$ is found (9-21)% and (21–30)% higher than the base channel geometry and optimized$_{RMS}$ channel geometries, respectively, on the cold side. Simultaneously, the friction factor for the optimizedML is found (6-21)% and (19–30)% higher on the hot side than the base and optimized$_{RMS}$ channel, respectively. However, the friction factor values of the optimized$_{ML}$ were found to be significantly lower than the zigzag channel geometries, i.e., (12–42) % on the hot side and (34–74) % on the cold side.

Fig. 8c reveals a comparison of PEC of the C-shaped channel (base geometry), C-Shaped channel (optimized$_{RMS}$), and C-Shaped channel (optimized$_{ML}$) concerning the zigzag channel geometry. The confirm lines show the quantities on the cold side, and the dotted lines represent the flow on the hot side. The comparison suggests that the overall performance based on the PEC values of the optimized$_{ML}$ geometry is considerably superior compared to the conventional zigzag geometry, particularly at lower values of the Reynolds number. The maximum values of the PEC were computed as 1.24, 1.21, and 1.18 for the optimized$_{ML}$, optimized$_{RMS,}$ and C-shaped base channel geometry on the cold side. At the same time, corresponding quantities on the hot side were found 1.16, 1.6, and 1.11, respectively. The results suggest that the optimization process involving ML methods is more realistic and robust. optimized$_{ML}$

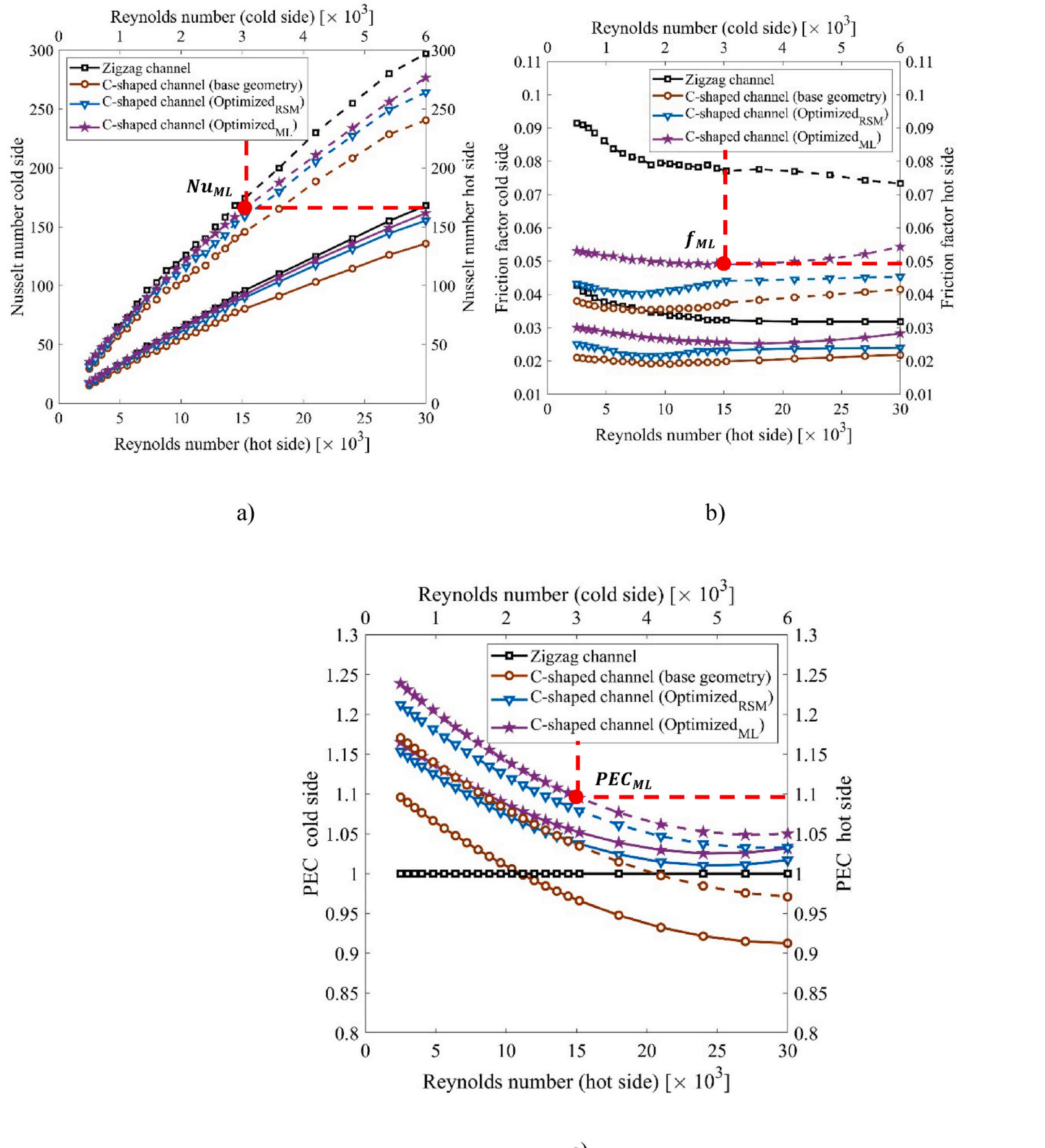

Fig. 8. a) Comparison of the Nusselt number for the zigzag channel, C-shaped channel (base geometry), C-Shaped channel (optimized$_{RMS}$), and C-Shaped channel (optimized$_{ML}$), b) Comparison of the friction factor for the zigzag channel, C-shaped channel (base geometry), C-Shaped channel (optimized$_{RMS}$), and C-Shaped channel (optimized$_{ML}$), c) Comparison of PEC of the C-shaped channel (base geometry), C-Shaped channel (optimizedRMS), and C-Shaped channel (optimizedML) concerning the zigzag channel geometry. The confirm lines show the quantities on the cold side, and the dotted lines represent the flow on the hot side.

5. Conclusion

In the current study, a C-shaped channel geometry has been optimized to improve the overall performance of the C-shaped PCHE. In this context, 81 channel geometries based on C-shaped fins were computed using 3D-RANS simulations. The generated data is used to train the various machine learning algorithms. Later, a trained ML model with the best performance is coupled with the multi-objective genetic algorithm to evaluate the optimal configuration of the design variables. Finally, the thermohydraulic characteristics of the optimized C-shaped channel geometry are assessed for a wide range of Reynolds numbers, and its performance is compared with the base design of the C-shaped channel and zigzag channel geometries. The following conclusions are withdrawn from the study:

- The sensitivity of the dependent variables Nu, f, and PEC to the independent ones has been investigated using the WLS method. It is discovered that Nu and f are responsive to all opted input parameters. It is found that the sensitivity of Nu to p_l and p_t is nearly identical and greatest among the other two input parameters. At the same time, f is highly sensitive to h and least susceptible to p_t.
- Deep neural networks DNN, XGBoost, and LGBM, have been used to predict Nu and f, where DNN shows the best performance among these three algorithms. It is found that the trained DNN model can estimate 99% of the Nusselt number and friction factor data with 98% confidence.
- A parametric design parameter analysis is performed using a trained deep neural network (DNN). It is found that the Nusselt number increases linearly with an increase in the value of fin depth (h), while a non-linearly drop in the value of Nu is observed with an increase in the values of the rest of the design variables, i.e., fin length (l_f), transverse pitch (p_t) and longitudinal pitch (p_l). On the other hand, the friction factor (f) and performance evaluation criteria (PEC) are found to be nonlinear functions of all design variables adopted for the current work.
- When coupled with the multi-objective genetic algorithm (DNN-MOGA), the deep neural network has proven to be more robust and effective than the previously used RSM-GA technique [33]. The comparison suggests that the overall performance based on the PEC values of the optimized$_{ML}$ geometry is considerably superior in comparison with the conventional zigzag geometry, particularly at lower values of the Reynolds number. The PEC value for the optimized$_{ML}$ geometry is found to be 1.24 and 1.14 on the cold and hot sides, respectively. Furthermore, the performance of the optimized$_{ML}$ geometry is found to be considerably higher (1.16 times) than the base design of the c-shaped channel geometry.
- The currently developed model can only be used for the C-shaped channel under the recuperator conditions. In future, models independent of the channel geometry and operating conditions can be developed. However, it would require huge computational time and resources initially to generate data for various channel geometries and under a wide range of operating conditions.

Author statement

Muhammad Saeed: Conceptualization, Data curation, Methodology, Software, Investigation, Visualization, Writing- Original draft preparation.

Abdallah Sofiane Berrouk: Formal Analysis, Writing- Original draft preparation, Supervision, Project Administration, Funding Acquisition.

Yasser F. Al Wahedi: Writing- Reviewing and Editing, Supervision, Project Administration.

Munendra Pal Singh: Visualization, Writing- Original draft preparation, Writing- Reviewing and Editing.

Ibragim Abu Dagga: Visualization, Software, Writing- Original draft preparation.

Imran Afgan: Visualization, Supervision.

Declaration of competing interest

The authors declare that they have no known competing financial interests or personal relationships that could have appeared to influence the work reported in this paper.

Acknowledgements

The authors acknowledge the financial support from Khalifa University of Science and Technology through grant No. CIRA-2019-031 and the Khalifa University of Science and Technology support through funding No. RC2-2018-024.

Appendix A: Methodology

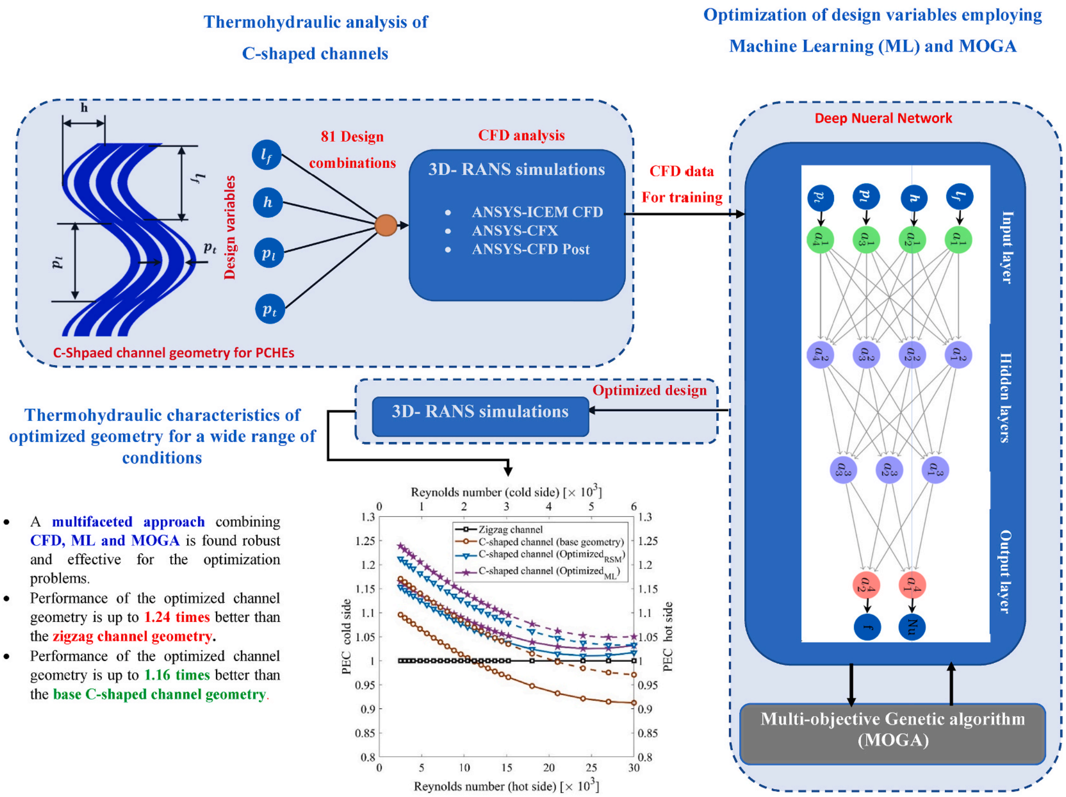

Appendix B: geometrical configuration studies

S.No.	Geometric configurations				CFD results		
	l_f [mm]	h [mm]	p_l [mm]	p_t [mm]	Nu	f	PEC
1	1.81	1.52	2.72	1.76	193.03	0.174	0.502
2	1.81	1.52	2.72	2.35	167.09	0.160	0.543
3	1.81	1.52	2.72	2.94	145.47	0.155	0.292
4	1.81	1.52	3.62	1.76	169.91	0.127	0.633
5	1.81	1.52	3.62	2.35	143.84	0.097	0.689
6	1.81	1.52	3.62	2.94	111.27	0.100	0.463
7	1.81	1.52	4.53	1.76	147.51	0.133	0.413
8	1.81	1.52	4.53	2.35	120.69	0.098	0.482
9	1.81	1.52	4.53	2.94	83.21	0.101	0.216
10	1.81	3.03	2.72	1.76	207.08	0.186	0.700
11	1.81	3.03	2.72	2.35	193.48	0.146	0.785
12	1.81	3.03	2.72	2.94	157.53	0.162	0.512
13	1.81	3.03	3.62	1.76	179.14	0.122	0.859
14	1.81	3.03	3.62	2.35	160.28	0.084	0.899
15	1.81	3.03	3.62	2.94	134.54	0.100	0.634
16	1.81	3.03	4.53	1.76	160.29	0.124	0.576
17	1.81	3.03	4.53	2.35	135.69	0.096	0.649
18	1.81	3.03	4.53	2.94	102.92	0.100	0.384
19	1.81	4.55	2.72	1.76	233.66	0.248	0.550
20	1.81	4.55	2.72	2.35	199.68	0.206	0.618
21	1.81	4.55	2.72	2.94	181.31	0.226	0.370
22	1.81	4.55	3.62	1.76	206.48	0.186	0.653
23	1.81	4.55	3.62	2.35	172.42	0.151	0.728
24	1.81	4.55	3.62	2.94	148.54	0.154	0.442
25	1.81	4.55	4.53	1.76	170.89	0.193	0.363
26	1.81	4.55	4.53	2.35	156.74	0.156	0.430
27	1.81	4.55	4.53	2.94	121.62	0.155	0.163
28	3.62	1.52	2.72	1.76	187.37	0.133	0.673

(continued on next page)

(*continued*)

S.No.	Geometric configurations				CFD results		
	l_f [mm]	h [mm]	p_l [mm]	p_t [mm]	Nu	f	PEC
29	3.62	1.52	2.72	2.35	153.48	0.104	0.759
30	3.62	1.52	2.72	2.94	123.32	0.108	0.505
31	3.62	1.52	3.62	1.76	144.19	0.074	0.876
32	3.62	1.52	3.62	2.35	124.42	0.038	0.950
33	3.62	1.52	3.62	2.94	94.46	0.050	0.666
34	3.62	1.52	4.53	1.76	117.98	0.076	0.659
35	3.62	1.52	4.53	2.35	98.56	0.046	0.705
36	3.62	1.52	4.53	2.94	68.39	0.058	0.460
37	3.62	3.03	2.72	1.76	191.77	0.130	0.883
38	3.62	3.03	2.72	2.35	168.23	0.092	0.965
39	3.62	3.03	2.72	2.94	147.93	0.102	0.695
40	3.62	3.03	3.62	1.76	175.88	0.071	1.019
41	3.62	3.03	3.62	2.35	150.39	0.037	1.088
42	3.62	3.03	3.62	2.94	117.99	0.042	0.802
43	3.62	3.03	4.53	1.76	144.45	0.074	0.810
44	3.62	3.03	4.53	2.35	114.60	0.044	0.849
45	3.62	3.03	4.53	2.94	89.82	0.048	0.583
46	3.62	4.55	2.72	1.76	214.58	0.188	0.705
47	3.62	4.55	2.72	2.35	186.75	0.153	0.745
48	3.62	4.55	2.72	2.94	165.92	0.156	0.476
49	3.62	4.55	3.62	1.76	189.17	0.129	0.821
50	3.62	4.55	3.62	2.35	163.78	0.101	0.881
51	3.62	4.55	3.62	2.94	134.50	0.109	0.616
52	3.62	4.55	4.53	1.76	158.98	0.132	0.535
53	3.62	4.55	4.53	2.35	128.46	0.102	0.614
54	3.62	4.55	4.53	2.94	104.20	0.103	0.335
55	5.43	1.52	2.72	1.76	152.54	0.144	0.472
56	5.43	1.52	2.72	2.35	132.13	0.105	0.545
57	5.43	1.52	2.72	2.94	102.12	0.111	0.308
58	5.43	1.52	3.62	1.76	124.32	0.083	0.677
59	5.43	1.52	3.62	2.35	100.48	0.043	0.768
60	5.43	1.52	3.62	2.94	70.23	0.053	0.493
61	5.43	1.52	4.53	1.76	102.54	0.081	0.491
62	5.43	1.52	4.53	2.35	72.94	0.051	0.551
63	5.43	1.52	4.53	2.94	46.32	0.064	0.314
64	5.43	3.03	2.72	1.76	182.54	0.135	0.645
65	5.43	3.03	2.72	2.35	156.05	0.104	0.700
66	5.43	3.03	2.72	2.94	124.74	0.105	0.447
67	5.43	3.03	3.62	1.76	150.20	0.078	0.815
68	5.43	3.03	3.62	2.35	115.87	0.040	0.882
69	5.43	3.03	3.62	2.94	92.87	0.049	0.626
70	5.43	3.03	4.53	1.76	111.77	0.082	0.617
71	5.43	3.03	4.53	2.35	91.62	0.047	0.663
72	5.43	3.03	4.53	2.94	60.44	0.054	0.410
73	5.43	4.55	2.72	1.76	193.32	0.183	0.425
74	5.43	4.55	2.72	2.35	171.20	0.162	0.469
75	5.43	4.55	2.72	2.94	140.93	0.170	0.223
76	5.43	4.55	3.62	1.76	160.55	0.136	0.546
77	5.43	4.55	3.62	2.35	140.61	0.098	0.635
78	5.43	4.55	3.62	2.94	109.21	0.103	0.346
79	5.43	4.55	4.53	1.76	139.42	0.135	0.328
80	5.43	4.55	4.53	2.35	108.26	0.101	0.380
81	5.43	4.55	4.53	2.94	75.48	0.109	0.110

Appendix C: Pareto Front data

S.No.	l_f [mm]	h [mm]	p_l [mm]	p_t [mm]	Nu	f	PEC
1	3.64	3.48	3.36	2.15	164.88	0.05	1.09
2	3.54	3.30	3.52	2.22	153.65	0.04	1.09
3	3.51	3.52	3.43	2.06	169.01	0.06	1.09
4	3.45	3.19	3.39	2.25	157.24	0.04	1.09
5	3.46	3.19	3.55	2.15	156.01	0.04	1.08
6	3.50	3.55	3.35	2.05	173.29	0.06	1.08
7	3.57	3.23	3.64	2.19	148.98	0.04	1.08
8	3.51	3.15	3.62	2.18	150.25	0.04	1.07

(*continued on next page*)

(*continued*)

S.No.	l_f [mm]	h [mm]	p_l [mm]	p_t [mm]	Nu	f	PEC
9	3.49	3.02	3.55	2.28	146.78	0.04	1.07
10	3.49	3.57	3.23	2.04	178.10	0.07	1.07
11	3.61	3.17	3.55	2.34	143.90	0.04	1.07
12	3.43	3.50	3.31	1.94	180.62	0.07	1.07
13	3.49	3.23	3.49	1.86	175.03	0.07	1.06
14	3.68	3.57	3.15	1.88	186.63	0.08	1.05
15	3.71	3.58	3.15	1.83	188.99	0.09	1.05
16	3.67	3.08	3.70	2.33	137.02	0.03	1.04
17	3.40	3.71	3.14	1.81	195.10	0.10	1.03
18	3.69	2.97	3.82	2.20	137.31	0.04	1.02
19	3.11	3.45	3.16	1.88	191.61	0.10	1.02
20	3.27	3.77	3.15	1.83	195.70	0.11	1.01
21	3.71	2.95	3.82	2.29	132.76	0.03	1.01
22	3.71	2.95	3.82	2.30	132.37	0.03	1.01
23	2.96	3.72	3.20	1.83	197.14	0.12	1.00
24	3.70	3.06	3.81	2.42	129.01	0.03	0.99
25	2.81	3.45	3.05	1.85	199.08	0.12	0.98
26	3.74	2.84	3.79	2.46	126.00	0.03	0.97
27	3.74	2.80	3.82	2.46	124.72	0.03	0.96
28	3.74	2.80	3.82	2.46	124.72	0.03	0.96
29	1.98	3.68	3.01	1.81	212.07	0.16	0.96
30	1.96	3.74	2.97	1.80	214.00	0.17	0.96
31	2.15	3.84	3.15	1.83	207.48	0.15	0.96
32	2.10	3.64	3.02	1.93	205.33	0.15	0.95
33	2.00	3.82	2.87	1.80	216.48	0.18	0.94
34	1.81	4.51	2.77	1.78	226.32	0.22	0.92
35	1.98	4.52	2.80	1.80	223.74	0.22	0.91

References

[1] Y. Ahn, S.J. Bae, M. Kim, S.K. Cho, S. Baik, J.I. Lee, J.E. Cha, Review of supercritical CO2 power cycle technology and current status of research and development, Nucl. Eng. Technol. 47 (2015) 647–661.

[2] Y. Khan, R. Shyam Mishra, Thermo-economic analysis of the combined solar based pre-compression supercritical CO2 cycle and organic Rankine cycle using ultra low GWP fluids, Therm. Sci. Eng. Prog. 23 (2021), 100925, https://doi.org/10.1016/j.tsep.2021.100925.

[3] Y. Feng, Z. Du, M. Shreka, Y. Zhu, S. Zhou, W. Zhang, Thermodynamic analysis and performance optimization of the supercritical carbon dioxide Brayton cycle combined with the Kalina cycle for waste heat recovery from a marine low-speed diesel engine, Energy Convers. Manag. 206 (2020), 112483, https://doi.org/10.1016/j.enconman.2020.112483.

[4] K. Brun, P. Friedman, R. Dennis (Eds.), Fundamentals and Applications of Supercritical Carbon Dioxide (sCO2) Based Power Cycles, Woodhead Publishing, 2017.

[5] M. Saeed, K. Alawadi, S.C. Kim, Performance of supercritical CO2 power cycle and its turbomachinery with the printed circuit heat exchanger with straight and zigzag channels, Energies 14 (2021), https://doi.org/10.3390/en14010062.

[6] M. Saeed, A.S. Berrouk, M. Salman Siddiqui, A. Ali Awais, Effect of printed circuit heat exchanger's different designs on the performance of supercritical carbon dioxide Brayton cycle, Appl. Therm. Eng. 179 (2020), 115758, https://doi.org/10.1016/j.applthermaleng.2020.115758.

[7] S. hui Liu, Y. ping Huang, J. feng Wang, R. long Liu, J. guang Zang, Experimental study of thermal-hydraulic performance of a printed circuit heat exchanger with straight channels, Int. J. Heat Mass Tran. 160 (2020) 1–12, https://doi.org/10.1016/j.ijheatmasstransfer.2020.120109.

[8] W. xiao Chu, X. hui Li, T. Ma, Y. tung Chen, Q. wang Wang, Experimental investigation on SCO2-water heat transfer characteristics in a printed circuit heat exchanger with straight channels, Int. J. Heat Mass Tran. 113 (2017) 184–194, https://doi.org/10.1016/j.ijheatmasstransfer.2017.05.059.

[9] M. Saeed, M.I. Radaideh, A.S. Berrouk, K. Alawadhi, Machine learning-based efficient multilayered precooler design approach for supercritical CO2 cycle, Energy Convers. Manag. X. 11 (2021), 100104, https://doi.org/10.1016/j.ecmx.2021.100104.

[10] N. Tsuzuki, Y. Kato, T. Ishiduka, High performance printed circuit heat exchanger, Appl. Therm. Eng. 27 (2007) 1702–1707, https://doi.org/10.1016/j.applthermaleng.2006.07.007.

[11] A. Meshram, A.K. Jaiswal, S.D. Khivsara, J.D. Ortega, C. Ho, R. Bapat, P. Dutta, Modeling and analysis of a printed circuit heat exchanger for supercritical CO2 power cycle applications, Appl. Therm. Eng. 109 (2016) 861–870, https://doi.org/10.1016/j.applthermaleng.2016.05.033.

[12] W. Chu, X. Li, Y. Chen, Q. Wang, T. Ma, Experimental study on small scale printed circuit heat exchanger with zigzag channels, Heat Tran. Eng. 42 (2021) 723–735, https://doi.org/10.1080/01457632.2020.1735779.

[13] S. Jeon, Y.-J. Baik, C. Byon, W. Kim, Thermal performance of heterogeneous PCHE for supercritical CO2 energy cycle, Int. J. Heat Mass Tran. 102 (2016) 867–876, https://doi.org/10.1016/j.ijheatmasstransfer.2016.06.091.

[14] S.-M. Lee, K.-Y. Kim, Comparative study on performance of a zigzag printed circuit heat exchanger with various channel shapes and configurations, Heat Mass Tran. 49 (2013) 1021–1028, https://doi.org/10.1007/s00231-013-1149-4.

[15] J. Figley, X. Sun, S.K. Mylavarapu, B. Hajek, Numerical study on thermal hydraulic performance of a printed circuit heat exchanger, Prog. Nucl. Energy 68 (2013) 89–96, https://doi.org/10.1016/j.pnucene.2013.05.003.

[16] W. Kim, Y.-J. Baik, S. Jeon, D. Jeon, C. Byon, A mathematical correlation for predicting the thermal performance of cross, parallel, and counterflow PCHEs, Int. J. Heat Mass Tran. 106 (2017) 1294–1302, https://doi.org/10.1016/j.ijheatmasstransfer.2016.10.110.

[17] X. hui Li, T. rui Deng, T. Ma, H. bing Ke, Q. wang Wang, A new evaluation method for overall heat transfer performance of supercritical carbon dioxide in a printed circuit heat exchanger, Energy Convers. Manag. 193 (2019) 99–105, https://doi.org/10.1016/j.enconman.2019.04.061.

[18] Z. Rao, T. Xue, K. Huang, S. Liao, Multi-objective optimization of supercritical carbon dioxide recompression Brayton cycle considering printed circuit recuperator design, Energy Convers. Manag. 201 (2019), 112094, https://doi.org/10.1016/j.enconman.2019.112094.

[19] S. Tang, Ling-Hong, BO-Hao Yang, Jie Pan, Bengt, Thermal performance analysis in a zigzag channel printed circuit heat exchanger under different conditions, Heat Tran. Eng. (2021) 1–18, https://doi.org/10.1080/01457632.2021.1896832.

[20] C. Huang, W. Cai, Y. Wang, Y. Liu, Q. Li, B. Li, Review on the characteristics of flow and heat transfer in printed circuit heat exchangers, Appl. Therm. Eng. 153 (2019) 190–205, https://doi.org/10.1016/J.APPLTHERMALENG.2019.02.131.

[21] P. Behnam, M. Faegh, M.B. Shafii, M. Khiadani, A comparative study of various machine learning methods for performance prediction of an evaporative condenser, Int. J. Refrig. 126 (2021) 280–290, https://doi.org/10.1016/j.ijrefrig.2021.02.009.
[22] S. Uguz, O. Ipek, Prediction of the parameters affecting the performance of compact heat exchangers with an innovative design using machine learning techniques, J. Intell. Manuf. (2021) 1–25, https://doi.org/10.1007/s10845-020-01729-0.
[23] J. Huang, T. Jin, M. Liang, H. Chen, Prediction of heat exchanger performance in cryogenic oscillating flow conditions by support vector machine, Appl. Therm. Eng. 182 (2021), 116053, https://doi.org/10.1016/j.applthermaleng.2020.116053.
[24] E.M.S. El-Said, M. Abd Elaziz, A.H. Elsheikh, Machine learning algorithms for improving the prediction of air injection effect on the thermohydraulic performance of shell and tube heat exchanger, Appl. Therm. Eng. 185 (2021), 116471, https://doi.org/10.1016/j.applthermaleng.2020.116471.
[25] G.A. Longo, S. Mancin, G. Righetti, C. Zilio, R. Ceccato, L. Salmaso, Machine learning approach for predicting refrigerant two-phase pressure drop inside Brazed Plate Heat Exchangers (BPHE), Int. J. Heat Mass Tran. 163 (2020), 120450, https://doi.org/10.1016/j.ijheatmasstransfer.2020.120450.
[26] L. Zhou, D. Garg, Y. Qiu, S.M. Kim, I. Mudawar, C.R. Kharangate, Machine learning algorithms to predict flow condensation heat transfer coefficient in mini/micro-channel utilizing universal data, Int. J. Heat Mass Tran. 162 (2020), 120351, https://doi.org/10.1016/j.ijheatmasstransfer.2020.120351.
[27] D. Shi, L. Sun, Y. Xie, Off-design performance prediction of a S-CO2 turbine based on field reconstruction using deep-learning approach, Appl. Sci. 10 (2020), https://doi.org/10.3390/app10144999.
[28] M. Saeed, A.S. Berrouk, B.M. Burhani, A.M. Alatyar, Y.F. Al Wahedi, Turbine design and optimization for a supercritical CO_2 cycle using a multifaceted approach based on deep neural network, Energies 14 (22) (2021), https://doi.org/10.1016/j.enconman.2020.113375.
[29] S. Son, Y. Jeong, S.K. Cho, J.I. Lee, Development of supercritical CO2 turbomachinery off-design model using 1D mean-line method and Deep Neural Network, Appl. Energy 263 (2020), 114645, https://doi.org/10.1016/j.apenergy.2020.114645.
[30] M. Saeed, M.-H. Kim, Thermal-hydraulic analysis of sinusoidal fin-based printed circuit heat exchangers for supercritical CO2 Brayton cycle, Energy Convers. Manag. 193 (2019) 124–139, https://doi.org/10.1016/j.enconman.2019.04.058.
[31] A. Massimiani, L. Palagi, E. Sciubba, L. Tocci, Neural networks for small scale ORC optimization, Energy Proc. 129 (2017) 34–41, https://doi.org/10.1016/j.egypro.2017.09.174.
[32] G. Villarrubia, J.F. De Paz, P. Chamoso, F. De la Prieta, Artificial neural networks used in optimization problems, Neurocomputing 272 (2018) 10–16, https://doi.org/10.1016/j.neucom.2017.04.075.
[33] M. Saeed, M.-H. Kim, Thermal-hydraulic analysis of sinusoidal fin-based printed circuit heat exchangers for supercritical CO2 Brayton cycle, Energy Convers. Manag. 193 (2019) 124–139, https://doi.org/10.1016/j.enconman.2019.04.058.
[34] M. Saeed, A.S. Berrouk, M. Salman Siddiqui, A. Ali Awais, Numerical investigation of thermal and hydraulic characteristics of sCO_2-water printed circuit heat exchangers with zigzag channels, Energy Convers. Manag. 224 (2020), 113375, https://doi.org/10.1016/j.enconman.2020.113375. In this issue.
[35] ANSYS CFX, CFX-pre User's Guide Release 16.0, 2015.
[36] D.E. Kim, M.H. Kim, J.E. Cha, S.O. Kim, Numerical investigation on thermal-hydraulic performance of new printed circuit heat exchanger model, Nucl. Eng. Des. 238 (2008) 3269–3276.
[37] A. Meshram, A.K. Jaiswal, S.D. Khivsara, J.D. Ortega, C. Ho, R. Bapat, P. Dutta, Modeling and analysis of a printed circuit heat exchanger for supercritical CO2 power cycle applications, Appl. Therm. Eng. 109 (2016) 861–870, https://doi.org/10.1016/j.applthermaleng.2016.05.033.
[38] A. Kruizenga, M. Anderson, R. Fatima, M. Corradini, A. Towne, D. Ranjan, Heat transfer of supercritical carbon dioxide in printed circuit heat exchanger geometries, J. Therm. Sci. Eng. Appl. 3 (2011), 031002, https://doi.org/10.1115/1.4004252.
[39] M. Saeed, A.S. Berrouk, M.P. Singh, K. Alawadhi, M.S. Siddiqui, Analysis of supercritical CO_2 cycle using zigzag channel pre-cooler : a design optimization study based on deep neural network, Energies 14 (19) (2021), 6227, https://doi.org/10.3390/en14196227. In this issue.
[40] M. Saeed, A.S. Berrouk, M.S. AlShehhi, Y.F. AlWahedi, Numerical investigation of the thermohydraulic characteristics of microchannel heat sinks using supercritical CO2 as a coolant, J. Supercrit. Fluids 176 (2021), 105306, https://doi.org/10.1016/j.supflu.2021.105306.
[41] M. Saeed, M.-H. Kim, Aerodynamic performance analysis of an airborne wind turbine system with NREL Phase IV rotor, Energy Convers. Manag. 134 (2017) 278–289, https://doi.org/10.1016/j.enconman.2016.12.021.
[42] M. Saeed, A. Ali Awais, A.S. Berrouk, CFD aided design and analysis of a precooler with zigzag channels for supercritical CO 2 power cycle, Energy Convers. Manag. 236 (2021), 114029, https://doi.org/10.1016/j.enconman.2021.114029. In this issue.
[43] M. Saeed, M.-H. Kim, Thermal and hydraulic performance of SCO_2 PCHE with different fin configurations, Appl. Therm. Eng. 127 (2017) 975–985, https://doi.org/10.1016/j.applthermaleng.2017.08.113.
[44] T. Ishizuka, Y. Kato, Y. Muto, K. Nikitin, N.L. Tri, H. Hashimoto, Thermal–hydraulic characteristic of a printed circuit heat exchanger in a supercritical CO2 loop, in: 11th Int. Top. Meet. Nucl. React. Therm., Avignon, France, 2005.
[45] M. Saeed, M.-H. Kim, Thermal and hydraulic performance of SCO2 PCHE with different fin configurations, Appl. Therm. Eng. 127 (2017) 975–985, https://doi.org/10.1016/j.applthermaleng.2017.08.113.
[46] M.S. Siddiqui, M.H. Khalid, R. Zahoor, F.S. Butt, M. Saeed, A.W. Badar, A numerical investigation to analyze effect of turbulence and ground clearance on the performance of a roof top vertical–axis wind turbine, Renew. Energy 164 (2021), https://doi.org/10.1016/j.renene.2020.10.022.
[47] V.D. Zimparov, N.L. Vulchanov, Performance evaluation criteria for enhanced heat transfer surfaces, Int. J. Heat Mass Tran. 37 (1994) 1807–1816, https://doi.org/10.1016/0017-9310(94)90069-8.
[48] S.G. Kandlikar, S. Garimella, D. Li, S. Colin, M.R. King, Heat transfer and fluid flow in minichannels and microchannels. https://doi.org/10.1016/B978-0-08-098346-2.00002-8, 2014.
[49] D.E. Rumelhart, G.E. Hinton, R.J. Williams, Learning representations by back-propagating errors, Nature 323 (1986) 533–536, https://doi.org/10.1038/323533a0.
[50] E. Elbeltagi, T. Hegazy, D. Grierson, Comparison among five evolutionary-based optimization algorithms, Adv. Eng. Inf. 19 (2005) 43–53, https://doi.org/10.1016/j.aei.2005.01.004.
[51] H. Mo, H. Sun, J. Liu, S. Wei, Developing window behavior models for residential buildings using XGBoost algorithm, Energy Build. 205 (2019), 109564, https://doi.org/10.1016/j.enbuild.2019.109564.
[52] T. Chen, C. Guestrin, XGBoost: a scalable tree boosting system, in: Proc. ACM SIGKDD Int. Conf. Knowl. Discov, . Data Min., 2016, pp. 785–794, https://doi.org/10.1145/2939672.2939785.
[53] Z. Chu, J. Yu, A. Hamdulla, LPG-model: a novel model for throughput prediction in stream processing, using a light gradient boosting machine, incremental principal component analysis, and deep gated recurrent unit network, Inf. Sci. 535 (2020) 107–129, https://doi.org/10.1016/j.ins.2020.05.042.
[54] J.H. Holland, Adaptation in Natural and Artificial Systems: an Introductory Analysis with Applications to Biology, Control, and Artificial Intelligence. Complex Adaptive Systems, John H. Holland, MIT press, 1994, https://doi.org/10.1086/418447.
[55] M. Saeed, M.H. Kim, Thermal-hydraulic analysis of sinusoidal fin-based printed circuit heat exchangers for supercritical CO2 Brayton cycle, Energy Convers. Manag. 193 (2019) 124–139, https://doi.org/10.1016/j.enconman.2019.04.058.
[56] K. Wang, Y.L. He, Thermodynamic analysis and optimization of a molten salt solar power tower integrated with a recompression supercritical CO2 Brayton cycle based on integrated modeling, Energy Convers. Manag. 135 (2017) 336–350, https://doi.org/10.1016/j.enconman.2016.12.085.
[57] X. Shen, H. Yang, J. Chen, X. Zhu, Z. Du, Aerodynamic shape optimization of non-straight small wind turbine blades, Energy Convers. Manag. 119 (2016) 266–278, https://doi.org/10.1016/j.enconman.2016.04.008.
[58] Richard Dawkins, N. Davis, The Selfish Gene, Macat Library, 2017, https://doi.org/10.4324/9781912281251.
[59] J. Kennedy, Particle swarm: social adaptation of knowledge, in: Proc. IEEE Conf. Evol. Comput. ICEC, IEEE, 1997, pp. 303–308, https://doi.org/10.1109/icec.1997.592326.

[60] M. Dorigo, V. Maniezzo, A. Colorni, Ant system: optimization by a colony of cooperating agents, IEEE Trans. Syst. Man, Cybern. Part B. 26 (1996) 29–41.
[61] M. Dorigo, L.M. Gambardella, Ant colonies for the travelling salesman problem, Biosystems 43 (1997) 73–81, https://doi.org/10.1016/S0303-2647(97)01708-5.
[62] S.-Y. Liong, M. Atiquzzaman, Optimal design of water distribution network using shuffled complex evolution, J. Inst. Eng. 44 (2004) 93–107.